Three-Dimensional Flow Measurements in a Static Mixer

R. T. M. Jilisen, P. R. Bloemen, and M. F. M. Speetjens
Energy Technology Laboratory, Dept. of Mechanical Engineering, Eindhoven University of Technology,
P.O. Box 513, 5600 MB Eindhoven, The Netherlands

DOI 10.1002/aic.13935
Published online October 18, 2012 in Wiley Online Library (wileyonlinelibrary.com).

Laminar heat and mass transfer are central to a wide range of industrial processes, encompassing (thermal) processing of viscous fluids, compact equipment for process intensification, and emerging microfluidic devices. Many of these applications incorporate the ''static-mixing principle'' (stirring of a throughflow by internal elements) for mixing and heat-transfer enhancement. Investigations on static mixers primarily concern numerical simulations. Experimental studies, on the other hand, are relatively rare and to date restricted to visualization of mixing patterns or integral quantities as for example, pressure drop and heat-transfer coefficients. The present study expands on this by quantitative experimental analysis of three-dimensional (3-D) flow fields and streamline patterns in a representative static mixer using 3-D particle-tracking velocimetry. This necessitates tackling of (internal) refractions and reflections caused by the complex mixer geometry. Comparison of experimental results with numerical predictions reveals a good agreement. © 2012 American Institute of Chemical Engineers *AIChE J,* 59: 1746–1761, 2013
Keywords: fluid mechanics, mixing, 3-D velocimetry

Introduction

Heat and mass transfer under laminar flow conditions are key to a wide variety of industrial fluids-engineering processes of size extending from microns to meters. Examples range from the traditional (and still very relevant) mixing and thermal processing of viscous fluids[1–7] via compact processing equipment[8,9] down to the rapidly expanding field of microfluidic applications.[10–12] Many of these applications, notwithstanding their great diversity, operate by the ''static-mixing principle'': a (pressure-driven) continuous throughflow that is stirred in transverse direction via fixed internal elements to accomplish efficient heat transfer and/or mixing.[13] This continuous-processing mode in fact is one of the key elements in process intensification, a growing trend in industry, by compact and micro-scale equipment.[14–16]

Scientific studies on static mixers primarily concern numerical simulations and predominantly concentrate on the well-known Kenics mixer.[5,6,17–20] Experimental investigations of static mixers are, on the other hand, scarce and hitherto restricted to visualization of mixing patterns and either integral or local quantities as for example, pressure drop, residence-time distributions, mean heat-transfer coefficients, and wall shear stress.[7,21–25] Quantitative experimental analyses on truly three-dimensional (3-D) flow and mixing properties within static mixers are to the best of our knowledge nonexistent to date. This motivates the present study on 3-D flow measurements in a representative industrial static mixer by way of 3-D particle tracking velocimetry (3-DPTV). To this end, the 3-DPTV method developed at the Institute of Environmental Engineering, ETH Zürich, Switzerland is used.[26–28] This method has, within the scope of industrial mixing, found application before in the experimental investigation of stirred rectangular tanks.[29] Principal aim of this study is performance of truly 3-D velocimetry in a representative static mixer so as to pave the way to in-depth experimental analyses of industrial mixing processes.

Flow studies using 3-DPTV are to date restricted to relatively simple flow domains: rectangular tanks[27–33]; the interior of a cylindrical domain viewed directly through its flat endwalls[34,35] or indirectly through an enclosing rectangular viewing box.[36] However, static mixers are of far greater geometrical complexity on grounds of the cylindrical boundary and the presence of internal elements. This introduces two optical distortions, namely, refraction and reflection at curved and internal walls, which dramatically deteriorate the tracking performance and reliability. Tackling of these optical effects is essential for the 3-DPTV procedure to reliably determine the 3-D flow field and associated 3-D fluid trajectories. Refraction is reduced to an acceptable level by placement of the domain of interest in a cubical viewing box in an approach similar as adopted in Walpot et al.[36] Reflections are eliminated by utilization of fluorescent tracer particles, enabling their optical separation from reflections of the light source, based on the course of action pursued by Pedocchi et al.[37] and Blaj et al.[38]

The backbone of the proposed measurement strategy is the particular combination of the above optical techniques with the 3-DPTV method introduced before. Its performance is evaluated by comparison of experimental results with numerical simulations and concentrates on two properties relevant to mixing: (1) the 3-D velocity field and (2) coherent structures that form in the 3-D streamline pattern due to continuity. The latter impose geometrical constraints on the fluid

Correspondence concerning this article should be addressed to M. F. M. Speetjens at m.f.m.speetjens@tue.nl.

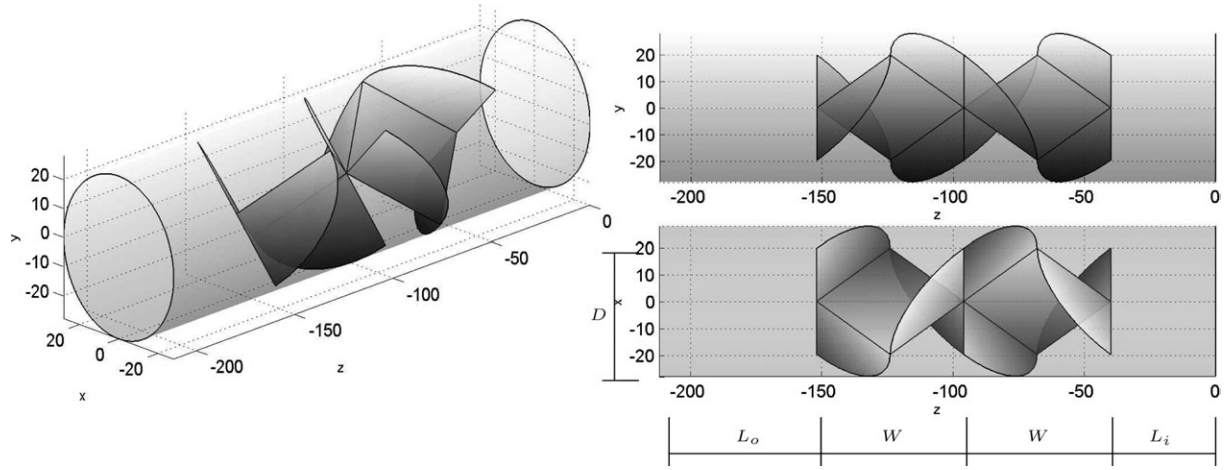

Figure 1. Mixer geometry including inlet and outlet tubes from various perspectives.

The axial throughflow takes place in negative *z*-direction. (Dimensions are in mm.)

motion and, thus, fundamentally determine the transport and mixing properties of a flow.[4,34,39]

The discussion hereafter is organized as follows. Section *Representative Case Study and Numerical Methods* introduces the industrial static mixer, adopted as representative case study, and the numerical methods used for flow simulations and data analysis. These simulations serve as reference for quantitative evaluation of the experimental results. The laboratory setup and the experimental techniques are treated in section *Experimental Methods*. Section *General Tracking Performance* elaborates on the general tracking performance of the measurement procedure. Section *Measurement of 3-D Flow Field and 3-D Streamline Pattern* is dedicated to its application for experimental characterization of 3-D flow fields and 3-D streamline patterns and includes a comparative analysis with numerical predictions. Conclusions are drawn and an outlook to follow-up studies is offered in section *Conclusions*.

Representative Case Study and Numerical Methods

The subject of investigation is a representative industrial static mixer, namely, the so-called Q-type mixer (Primix BV, Mijdrecht, The Netherlands), with a circular cross-section of diameter D that operates on the principle of systematic transverse reorientation of an axial throughflow by way of internal elements. The 3-D frame of reference is defined such that (x,y)-plane and z-direction correspond with transverse and axial directions, respectively. The internal elements consist of chevron-shaped central plates of width $D =$ 56 mm and length $L = D = 56$ mm with perpendicular elliptical segments extending to the outer cylinder wall. These elements are placed in succession and alternately axial-wise reversed and rotated over an angle of $\Theta = \pm\pi/4$ with the x axis, thus, resulting in a downstream periodic repetition of pairs of consecutive mixing elements shown in Figure 1. In this study, only this first pair of elements is considered. The flow domain is completed by inlet and outlet tubes of length $L_i = 40$ mm and $L_o = 60$ mm, respectively, resulting in a total axial extent of $L_{tot} = L_i + 2W + L_o = 212$ mm. The axial throughflow takes place in negative z-direction.

The flow is governed by the 3-D steady conservation laws for mass and momentum for an incompressible fluid, reading

$$\nabla \cdot u = 0, \quad \rho u \cdot \nabla u = -\nabla p + \mu \nabla^2 u \tag{1}$$

with u is the fluid velocity, p the static pressure, ρ the fluid density, and μ the dynamic fluid viscosity. Dimensional analysis based on the scaling $x = Dx'$, $u = Uu'$, $p = Pp'$, with U a characteristic velocity and $P = \mu U/D$, where primes indicate dimensionless variables, yields

$$\mathrm{Re} = \frac{\rho U D}{\mu}, \quad \Lambda = \frac{L}{D} \tag{2}$$

as relevant nondimensional parameters. Here, Re and Λ represent the well-known Reynolds number and the aspect ratio of the mixing elements, respectively. The geometrical parameter is in the configuration according to Figure 1 fixed at $\Lambda = 1$, implying square central plates within each mixing element. The case study hereafter uses water ($\rho = 1000$ kg/m^3 and $\mu = 1.0 \cdot 10^{-3}$ Pa s^{-1}) as working medium at a given flow rate of $\phi = 80$ l/h, resulting in a mean inlet velocity of $U = 9$ mm/s and advancing a Reynolds number of $Re = 505$ (section *Laboratory set-up*). The close resemblance of the present geometry to the Kenics mixer, which has a threshold to transition at $Re \approx 1000$,[5] implies a laminar flow here. This *a posteriori* justifies the above pressure scaling based on a balance primarily between viscous forces and pressure gradients.

Numerical reference data are obtained by numerical simulation of the flow field within the mixer by the commercial computational fluid dynamics (CFD) package ANSYS-FLUENT (double-precision implicit pressure-based solver for 3-D steady laminar flows; pressure-velocity coupling via SIMPLE scheme; second-order upwind scheme for convective term; convergence criterion residuals 10^{-12}). This strategy has in fact proven its worth in numerous computational analyses of static mixers.[5,18,20] Hence, the present study adopts essentially the same approach. The flow domain in Figure 1 is discretized by a computational mesh consisting of about $1.4 \cdot 10^6$ tetrahedral elements (maximum side length 2 mm). Standard grid-dependence tests determined this mesh as sufficient for adequate resolution of the flow. The no-slip condition $u = 0$ is imposed on the tube wall and the internal elements; the velocity profile is prescribed at the inlet $z = 0$ via the user-defined function option of ANSYS-FLUENT and isobaric conditions are presumed at the outlet $z = 212$ mm. The inlet profile is prescribed via actual

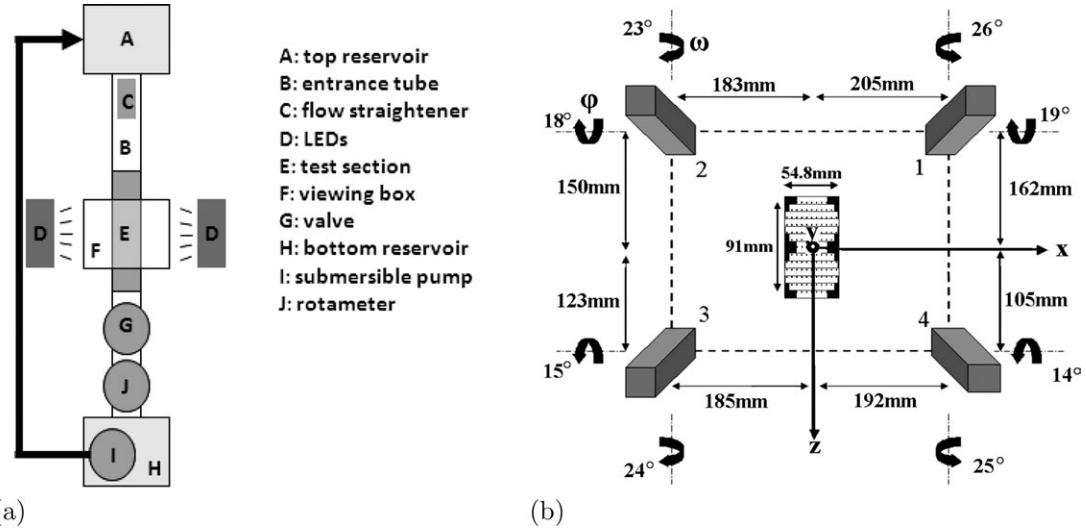

Figure 2. Laboratory facility: (a) schematic of the experimental setup; (b) camera configuration (grey boxes labeled 1–4) facing the calibration body (central object with projected area of 54.8 × 91 mm) as inserted in the test section E.

Distances in panel (b) indicate camera mounting positions relative to origin; angles indicate camera tilt about the horizontal (φ) and vertical (ω) axes.

experimental data (section *Laboratory set-up*) and corresponds with a fixed axial pressure drop that drives the throughflow. This ensures a close match between numerical model and laboratory conditions. Comparative analyses of numerical and experimental results are carried out by way of dedicated postprocessing tools implemented in the high-level programming language MATLAB.

Important to note is that the assumed steady behavior is a consequence of the laminar flow conditions. This is consistent with findings on the Kenics mixer[5,18,20] and has been verified for the present device via unsteady simulations starting from a stagnant fluid. This revealed a rapid transient toward a steady state throughout the entire flow domain. These steady conditions are in agreement with experimental observations (section *Measurement of 3-D Flow Field and 3-D Streamline Pattern*).

Experimental Methods

Laboratory set-up

Realistic operating conditions in actual industrial static mixers involve a steady continuous throughflow driven by a constant pressure gradient. In the laboratory setup, this situation is mimicked by placement of the mixer in a vertical configuration between two reservoirs and using the hydrostatic pressure as flow forcing. Figure 2a gives a schematic of this setup. The top reservoir A, via an entrance tube B (polyvinyl chloride (PVC); diameter 56 mm; length 560 mm) including a flow straightener C, releases water into the transparent test section E (glass; diameter 56 mm; wall thickness 2 mm) holding the transparent mixing elements (perspex; thickness 1.5 mm) that, through an outlet tube (PVC; diameter 56 mm) with valve G, is connected with the bottom reservoir H (indicated diameters are internal). Connector elements between entrance/outlet tubes and test section admit easy (dis)mounting of the latter for placement of mixing elements and insertion of the 3-DPTV calibration body (section *Data acquisition and data processing*). Test section E is enclosed by a glass viewing box F (200 × 200 × 200 mm) filled with water.

The pair of mixing elements is positioned in the test section E such that the inlet $z = 0$ of the mixer configuration (Figure 1) falls within the viewing box (and, thus, the field of view of the cameras). This enables measurement of the actual inlet velocity and, thus, adequate prescription of the inlet conditions (section *Representative Case Study and Numerical Methods*), which is essential for the numerical model. The total axial extent of $L_{tot} = 212$ mm exceeding the height of the viewing box means that a small part of the outlet region 152 mm $\leq z \leq$ 212 mm of the flow domain according to Figure 1 sits outside the measurement range. However, this is inconsequential for this study.

Two arrays of (in total 54) green light-emitting diodes (LEDs) D (LUXEON Rebel Color, Philips, The Netherlands) are fixed on two aluminium mounting frames and directed toward the test section from two opposite sides. The LEDs (intensity 180 lm at 700 mA) are equipped with collimator lenses to focus the light on the test section, and heat generated is released by cooling water circulating through the frames so as to maintain stable operating temperatures. Moreover, heat generation is minimized by operating the LEDs in pulsated mode, synchronized with the cameras. An array of four cameras, arranged in a configuration as shown in Figure 2b, records the fluorescent polymethyl methacrylate (PMMA) tracer particles ($d_p = 50$ μm, $\rho_p = 1190$ kg/m^3; Microparticles GmbH, Germany) flowing through the test section. Cameras and tracking algorithms—including the calibration body shown in Figure 2b—are discussed in more detail in section *Data acquisition and data processing*. Enclosure of the test section in the viewing box as well as the particular choice of light source and tracer particles serve to eliminate—or at least reduce—detrimental optical effects that degrade the image quality and compromise the performance of the image-processing software. Tackling these optical issues is essential for successful measurements in the current system. The adopted solutions are elaborated in section *Optical issues and their solution*.

Estimation of the particle dynamics yields $\tau_p = d_p^2\rho_p/18$ $\mu = 0.17$ ms as typical response time to acceleration of fluid parcels and $U_p = |\rho - \rho_p|gd_p^2/18$ $\mu = 0.26$ mm/s as typical

drift velocity due to buoyancy.[40] The former is negligible compared to the typical time scale $\tau_a = D/U = 6.22$ s of the flow, quantified by the particle Stokes number $St \equiv \tau_p/\tau_a \sim \mathcal{O}(10^{-5})$, meaning that particles virtually instantaneously follow deacceleration/acceleration of fluid parcels. (Here, τ_a is based on the large-scale vortical mixing structures.) The drift velocity is well below the fluid velocity, that is, $U_p/U \sim \mathcal{O}(10^{-2})$, and may give rise to a typical particle deviation $\Delta x_p \equiv U_p \tau_a \sim \mathcal{O}(1$ mm), from fluid trajectories during its residence within the test section. This is considered acceptable in the present context, because mixing properties of laminar flows are examined on the basis of coherent structures formed by clusters of fluid trajectories instead of in terms of individual trajectories (section *Internal 3-D streamline pattern*).

Reservoir water levels—and, thus, the hydrostatic pressure drop—are maintained constant by recirculating the outflow via a standard submersible pump I (Gamma Building Centers, The Netherlands). The flow rate ϕ and, inherently, the pressure drop over the mixer, is regulated by valve J in the outflow tube and monitored by rotameter J (Fischer and Porter, USA). This flow-regulation principle can be illustrated by way of Bernoulli's equation, yielding $\phi \sim A\sqrt{\rho g H + p_{amb} - p_{valve}}$, with H the height between the water levels, p_{amb} the ambient pressure, and $p_{valve} \geq p_{amb}$ the static pressure at the valve. This relation, though strictly invalid in the present case of laminar flow, exposes the general trend that ϕ increases with decreasing valve pressure p_{valve} (effectuated by variation of the flow cross-section) and vice versa. For the cases considered in this study, the flow rate is fixed at $\phi = 80$ L/h, resulting in a mean axial velocity of $U = \phi/A = 9$ mm/s, with A the cross-sectional area of the open tube, and a Reynolds number $Re = 505$.

The entrance tube E is of insufficient length (560 mm) to enable full development of the inlet flow into a Poiseuille profile; this requires for given conditions and Newtonian fluids an entrance length $L_e \approx 1.45\ m$ using $L_e/D = 0.59 + 0.05$ Re as correlation.[41] However, this is immaterial in present study, because the numerical model prescribes the measured inlet profile (section *Representative Case Study and Numerical Methods*). Moreover, entrance lengths are typically below L_e in realistic settings as well.

Data acquisition and data processing

Camera Configuration and Data Storage. The camera configuration is shown schematically in Figure 2b and records the tracer particles flowing through the test section from different perspectives. This arrangement is essential for determination of the 3-D positions of individual particles (section *3-D Particle-Tracking Algorithm*). The four cameras (MegaPlus ES2020, Kodak, United Kingdom) are mounted on a rigid frame with connectors that admit easy adjustment of position and viewing angle; 50 mm lenses (type NMV-50M1, Navitar, USA) including diaphragm ($f_{stop} \leq 16$) ensure optimal image quality (section *General Tracking Performance*). The cameras offer 12-bit sensitivity ($2^{12} = 4096$ intensity levels), a resolution of $W \times H = 1600 \times 1200$ pixels at a physical pixel size of $d_{pix} = 7.4\ \mu m^2$, and a maximum recording rate of 30 frames per second. Camera control, including synchronization for simultaneous recording, and data storage (240 MB/s at maximum sampling rate) are accomplished through a data-acquisition system (DVCR5000, Iris Vision, The Netherlands).

3D Particle-Tracking Algorithm. The basic principle of PTV is reconstruction of the trajectories and velocities of small tracer particles, seeded in the flow, from recordings of their motion by way of a camera. This, under the premise of tracers closely following fluid parcels, yields an accurate representation of the actual fluid trajectories and fluid velocity. Primary objective of PTV algorithms is isolation of the consecutive positions

$$\mathcal{X}_p = [x_p(0), x_p(\Delta t), x_p(2\Delta t), ...] \tag{3}$$

of physical particles p from subsequent images recorded at time levels $t = 0$, Δt, $2\Delta t$, … by way of so-called matching algorithms. The string of positions $\mathcal{X}_p$ directly gives the particle trajectory and, by interpolation schemes of the type

$$u_p(x_*, t) = \frac{x_p(t+\Delta t) - x_p(t)}{\Delta t}, \qquad x_* = \frac{x_p(t+\Delta t) + x_p(t)}{2} \tag{4}$$

enables evaluation of the corresponding velocity at positions x_*. Performing this for all tracer particles yields trajectories and velocity vectors throughout the flow domain.

Standard 2-DPTV reconstructs particle trajectories within 2-D flow domains from images recorded by a single camera. Reconstruction of 3-D trajectories, on the other hand, requires at least two cameras to determine, besides the particle position within the camera plane, also the distance in normal direction.[42] This so-called "stereoscopic reconstruction" is illustrated by the configuration shown in Figure 3a. Two cameras with focal length s are positioned at locations $X_{1,2}$ in the plane $z = 0$, facing an object at position (x_0,z_0) in the 2-D xz-space. This object appears at positions x_1 and x_2 in the image planes of Camera 1 and 2, respectively. Object position (x_0,z_0) and image positions $(x_{1,2})$ relate via

$$x_{1,2} = X_{1,2} + \frac{s(X_{1,2} - x_0)}{z_0 - s} \qquad \Leftrightarrow \qquad z_0 = \frac{s(x_{1,2} - x_0)}{x_1 - X_{1,2}} \tag{5}$$

revealing that tracers anywhere on the line $z_0 = a(x_{1,2})x_0 + b(x_{1,2})$ appear at one and the same image position $x_{1,2}$. (In Figure 3a, these lines correspond with the rays connecting image positions $x_{1,2}$ and object.) This has the important implication that, for known optical settings (s and $X_{1,2}$), each individual camera can from its recorded position $x_{1,2}$ only determine a line in space on which the object must sit yet not its exact position. However, the object is located at the intersection of lines of individual cameras, meaning that at least two lines—and, thus, at least two cameras—are sufficient to determine the exact position. The same principle as given in the simplified situation of Figure 3a holds in true 3-D space and its exploitation for 3-DPTV was first introduced by Chang and Taterson.[43] (Depth perception in human vision relies on exactly this optical principle, termed stereoscopic vision, explaining why we have two eyes.)[44] The principal reason for 3-DPTV algorithms to commonly use more than two cameras is to enhance the matching performance by enabling alternative combinations of image pairs in case matching fails for two given perspectives (e.g., due to limited optical accessibility). Correct matching of subsequent positions of a given physical particle namely is the key challenge in (3-D)PTV.[30,42]

This study adopts the 3-DPTV algorithm developed at ETH Zürich, Switzerland, which is freely available for noncommercial use.[26,27] The ETH algorithm leans on a geometrical-optics model of the generic configuration shown schematically in Figure 3b. It consists of cameras positioned

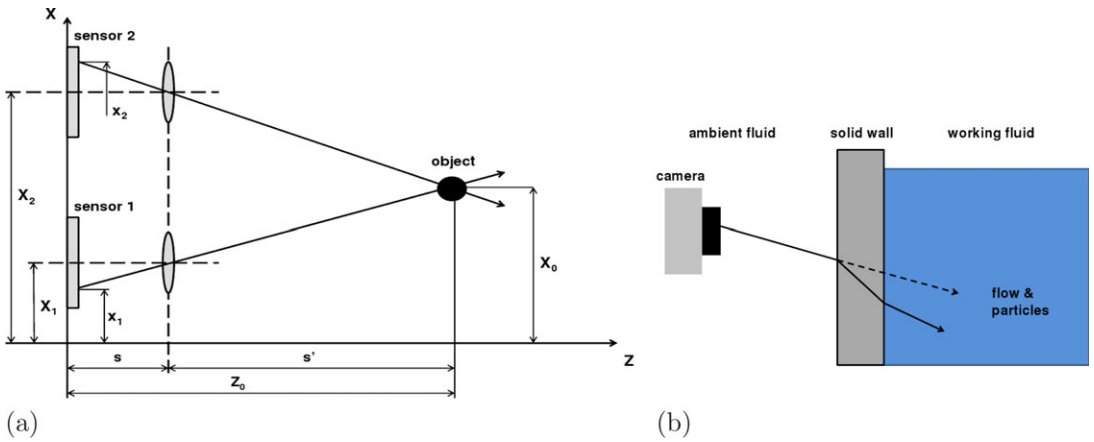

Figure 3. 3-D PTV: (a) basic working principle of 3-D position reconstruction from two 2-D camera images; (b) optical configuration modeled by the ETH 3-DPTV algorithm.

[Color figure can be viewed in the online issue, which is available at wileyonlinelibrary.com.]

outside a test section within a container with flat walls, causing light rays to undergo refraction at the two interfaces between ambient/working fluid and solid container wall. The optical model is in essence similar to that for the situation in Figure 3b yet takes a more complex form due to the 3-D reference frame and the refraction by the flat sidewalls of the rectangular container bounding the flow domain. Moreover, the ETH algorithm performs particle matching and stereoscopic trajectory reconstruction on the basis of four cameras. Hence, the four-camera configuration in the current laboratory setup.

Calibration of the Optical Model. Essential for determining 3-D particle positions from camera images is that the parameters of the optical model are known. For the simplified case in Figure 3, these parameters comprise the set (X_1,X_2,s); for the ETH algorithm, a similar set exists yet of larger size due to the greater complexity of the model. These parameters can in principle be determined directly from the camera configurations, their optical specifications, and the material properties of the container and the working fluid. However, this is a laborious and error-sensitive process. In practice, these parameters are, therefore, determined via calibration using a reference body with known dimensions. In case of the simplified model, a reference body with three marked positions, for example, bright dots on a black background, is sufficient to determine the three parameters (X_1,X_2,s). This connects positions $x_{1,2}$ in the image planes with positions (x_0,z_0) in the physical reference frame attached to the reference body and, thus, establishes the coordinate transformation between camera positions and physical positions. Calibration of the optical model in the ETH algorithm is accomplished in essentially the same way yet with the more elaborate reference body shown in Figure 4. It consists of a 3-D staircase-like black object (polyacetal) with a projected area of 54.8 $\times$ 91 mm^2 and covered by a grid of bright dots (diameter 1 mm). Transverse and length-wise grid spacings are 5 and 7.5 mm, respectively, within the projected area; offset between stairs is 7.5 mm. Calibration can be carried out either before or after an actual experiment and placement/removal of the reference body is facilitated by the dismountable test section. Note that the calibration configuration involves the reference body in the test section filled with the working fluid and, thus, is identical to the actual flow situation, save the internal elements. However, absence of the latter is inconsequential, as optical distortion by these elements is insignificant (section *Refraction at the Tube Wall and Internal Elements*).

Optical issues and their solution

Refraction at the Tube Wall and Internal Elements. The optical model of the ETH algorithm assumes a configuration

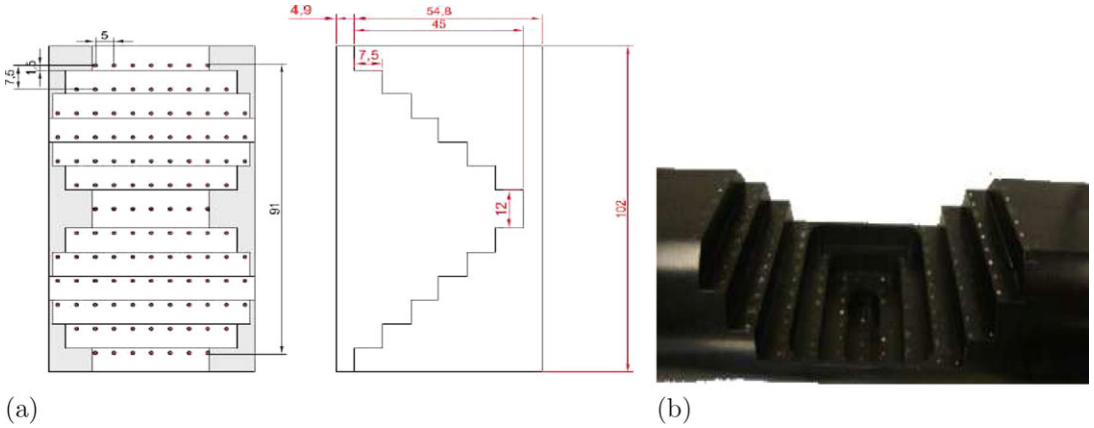

Figure 4. Calibration body for evaluating the model parameters of the ETH 3-DPTV algorithm: (a) dimensions and reference grid; (b) actual polyacetal calibration body.

[Color figure can be viewed in the online issue, which is available at wileyonlinelibrary.com.]

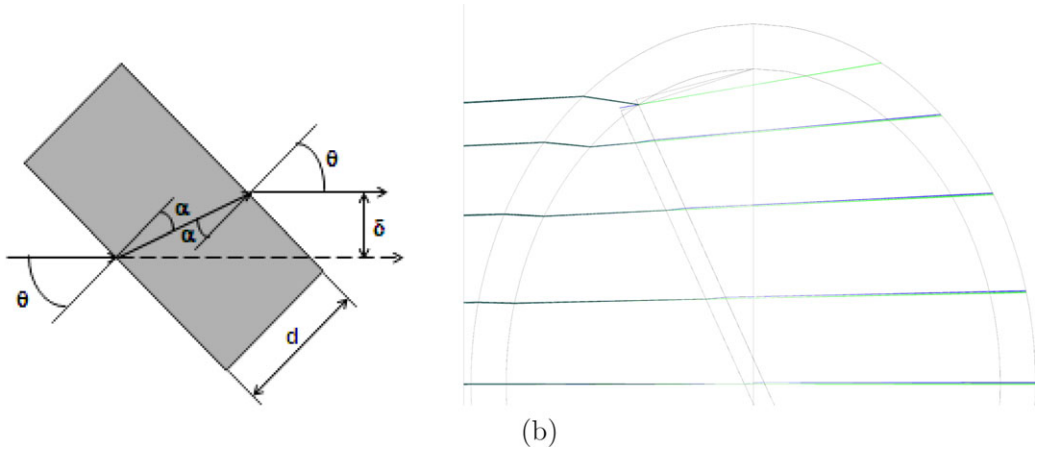

Figure 5. Optical distortion by refraction: (a) refraction of an incident light ray by an inclined flat wall; (b) unperturbed internal light rays (green) vs. internal light rays subject to refraction by the internal elements (blue).

[Color figure can be viewed in the online version, which is available at wileyonlinelibrary.com.]

according to Figure 3b comprising a single flat wall separating two different media. However, the mixer geometry itself consists of a tubular outer wall and internal elements, which is decidedly different. Hence, imagery obtained for this configuration can, strictly, not be handled by the ETH algorithm due to significant image distortion by refraction at the several (curved) interfaces. Placement of the test section inside a cubical viewing box filled with water (section *Laboratory set-up*) reduces internal refraction to acceptable levels and, thus, facilitates image processing with the ETH algorithm. This is based on the ansatz by Walpot et al.[36] and is discussed in more detail below.

Refraction of light by tube wall and internal elements is estimated by approximating the curved tube wall and internal elements by an inclined flat wall surrounded by a given fluid. The corresponding optical model is based on Snell's law and reads

$$\frac{\delta}{d} = \frac{\sin(\theta - \alpha)}{\cos\alpha}, \qquad \frac{\sin\alpha}{\sin\theta} = \frac{n_f}{n_s} \tag{6}$$

with configuration and variables according to Figure 5a.[44] Here, n_f and n_s are the associated refractive indices of fluid and solid wall, respectively. Measure for the optical distortion is the offset δ of the refracted ray relative to its unperturbed counterpart. The estimation takes $d_w = 2$ mm and $d_e = 1.5$ mm as thickness of the tube wall and internal element, respectively, $\theta = 45°$ as average angle of incidence and adopts $n_w = 1.33$ (water), $n_g = 1.51$ (glass), and $n_p = 1.00$ (perspex) as refractive indices. This yields $\delta \approx 0.3$ mm ($\delta/R \approx 1\%$) and $\delta \approx 0.2$ mm ($\delta/R \approx 0.7\%$) as offset by the tube wall and internal elements, respectively. These estimates offer first evidence in support of the assumption that remaining internal refraction within the test section is at acceptable levels and admits application of the ETH algorithm.

Simulation of the internal refraction by the commercial package ZEMAX-EE (Radiant Zemax LLC, USA) for optical-system design admits further examination. To this end, the full system including camera lenses (magnification factor: $-8.53\times$), viewing box, tube wall, and internal elements (represented by a wall positioned under 30° with the vertical) is modeled. Figure 5b shows the rays for the full system (blue) in contrast to those without internal element (green). Both sets of rays are nearly indistinguishable, signifying that refraction by the internal elements is negligible. Refraction of any significance is restricted to the localized region at the top of the tube and results from the strong increase in angle of incidence due to the wall curvature. Typical offsets amount to $\delta \approx 0.3$ mm ($\delta/R \approx 1\%$) and reach a maximum of $\delta \approx 0.8$ mm ($\delta/R \approx 3\%$) in the direct vicinity of the top of the tube. These computations closely correspond with the estimates made before and consolidate the earlier finding that the cubical viewing box reduces the optical distortion by internal refraction to an acceptable level for the ETH algorithm to be used for 3-DPTV.

Internal Reflections. The presence of curved and internal walls inside the test section introduces, besides the refraction discussed above, a further optical degradation of the imagery that must be tackled to admit 3-DPTV: reflections of the illuminating light rays on fluid-wall interfaces and small water-borne objects (e.g., air bubbles). These reflections may have an intensity that equals or even exceeds that of the light reflected by tracer particles. For instance, air bubbles, though usually sufficiently small to be harmless to the flow, are typically larger than tracer particles, reflecting a greater amount of light and, consequently, appearing at a higher intensity. Thus, visibility of tracer particles in the images may be insufficient for reliable detectablility and tracking. This phenomenon is remedied by utilization of fluorescent particles. Their key advantage over conventional particles is that they absorb the incident light from the light source and, instead of direct reflection, emit this at wavelengths different from that of the light source (and its reflections). This enables optical separation of reflections and fluorescence by an optical filter transparent only to the wavelength regime of the latter, causing only particles to emerge in the camera image. This filtering principle leans on a similar course of action as pursued before by, for example, Pedocchi et al.[37] and Blaj et al.[38] and is demonstrated in Figure 6a.

The present setup adopts green LEDs (intensity peak at $\lambda = 530$ nm) as light source in combination with PMMA particles doped with the fluorescent substance rhodamine B (section *Laboratory set-up*). Its absorption and emission peaks occur at $\lambda_{ab} = 560$ nm (green) and $\lambda_{em} = 585$ nm (red), respectively, and the quantum yield (fraction of

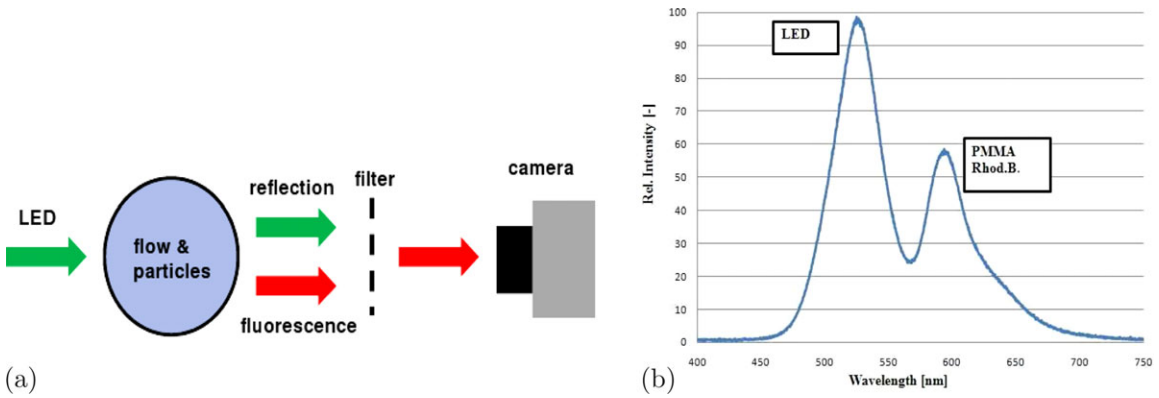

Figure 6. Optical separation of reflected LED light and fluorescence by the tracer particles: (a) basic filtering principle; (b) typical spectrum of light emanating from test section and its domination by the emission peaks of LEDs and rhodamine B-doped PMMA tracer particles.

[Color figure can be viewed in the online version, which is available at wileyonlinelibrary.com.]

absorbed light that is emitted via fluorescence) amounts to $\phi \approx 0.65$ at 25°C.[45] These properties ensure a strong fluorescence intensity at a wavelength that is sufficiently distinct from that of the light source. This is illustrated in Figure 6b, showing the spectral intensity distribution of a typical image of fluorescent particles inside the test section before optical filtering. Left and right peaks, respectively, correspond with refections of the LED light and the fluorescence by the particles. (Note that the relative peak intensities depend essentially on the dye concentration. The peak locations, on the other hand, are identical for any concentration. Only the latter is relevant for the optical separation.) The LED light includes contributions up to $\lambda = 620$ nm, meaning that reflections, though relatively weak, may nonetheless interfere with the fluorescence. Reflections are, therefore, suppressed by a two-stage optical filtering. First, the tail of the LED spectrum (above $\lambda \approx 570$ nm) is, before reaching the test section, eliminated by placement of cyan dichroic filters (FD1C, Thorlabs, Germany) on the collimator lenses; second, the strong reflections around the LED peak $\lambda = 530$ nm are eliminated from the light emerging from the test section by placement of a 590 nm high-pass filter (type OG-590, Schott Glass, Germany) before each camera lens.

General Tracking Performance

Circulation of water through the system is typically run for about 30 min to achieve stable and steady flow conditions and attain an even distribution of the fluorescent tracer particles. Images are recorded at the maximum recording rate of 30 frames per second and at an exposure time of 5 ms. This ensures a sufficient sampling frequency and recording intensity. Focal length $s = 50$ mm, maximum $f_{\text{stop}} = 16$, and mean distance $d_0 = 470$ mm from lens to calibration body yield $M = s/(d_0 - s) = 0.12$, as average magnification factor. This gives $Wd_{\text{pix}}/M \times Hd_{\text{pix}}/M = 100 \times 75$ mm^2, as field of view of the cameras, encompassing a region approximately the size of one mixing element, with a corresponding depth of field $2Hd_0^2/(H^2 - d_0^2) = 21$ mm, where $H = s^2/f_{\text{stop}}\, d_c$ is the hyperfocal distance and $d_c = d_{\text{pix}}$ is the circle of confusion.[46] Diffraction results in an effective particle diameter of $d_{\text{p,eff}} = \sqrt{(d_p M)^2 + d_{\text{diff}}^2} = 26.2\ \mu m \approx 3.5$ pixels, with $d_{\text{diff}} = 2.44 f_{\text{stop}}(M+1)\lambda_{\text{em}}$, on the CCD sensor.[40] One camera pixel corresponds with a projected physical area of about $60 \times 60\ \mu$m^2, meaning that particles have a typical displacement of 300 μm, or equivalently, 5-pixels, between subsequent frames. These optical properties constitute an optimal balance between maximum utilization of the camera resolution and facilitate reliable determination of particle location and motion.[40] Trajectories of individual particles can be measured only in flow regions within the fields of view. Hence, 3-D streamline portraits can be determined only for subregions of the flow domain. The velocity field, on the other hand, can be determined for the entire system. Its steady nature namely enables assembly of the velocity fields $u_{i,j}$ of individual time levels t_i ($i \in [0,N]$) and flow regions Ω_j ($j \in [0,M]$) into a high-density field covering the entire test section: $u_{\text{tot}} = u_{1,1} \cup u_{2,1} \cup \ldots \cup u_{i,j} \cup \ldots \cup u_{N,M}$. Experiments in the present study adopt this approach and paritition the flow domain into three regions: (1) "inlet region" including part of the upstream mixing element; (2) "mixing region" encompassing both mixing elements; and (3) "outlet region" including part of the downstream mixing element.

The effect of the optical filtering is demonstrated in Figure 7. Images without filtering (panel a) are dominated by reflections, rendering tracer particles nearly invisible. Filtering virtually removes these reflections and effectively isolates the tracer particles from the signal (panel b). (Note that here the dye concentration is substantially lower than in the sample shown in Figure 6b, causing a much greater intensity difference between reflections and fluorescence.) This dramatically improves the image quality and, in conjunction with reduction of internal refractions, is crucial for reliable and successful data processing with the ETH algorithm. Moreover, elimination of reflections also removes residual air bubbles from the images, thus, lowering the risk of nonphysical trajectories and spurious velocity vectors. Air bubbles, in contrast with the tracer particles, namely are subject to significant buoyancy and their motion, thus, poorly correlates with the fluid motion.

The general performance of the 3-DPTV algorithm is examined for measurement sessions in each of the regions specified above. Data acquisition has within each region been carried out for about 30–32 s, yielding some 900–960 images per camera and amounting to nearly 7.5 GB of data. On average, the 3-D positions $x_p(t_i)$ of 190 particles are identified from each set of images at a given time level t_i and an average matching yield of ~76% is attained. This generates nearly 6000 tracks $\mathcal{X}_p = [x_p(0), x_p(\Delta t), x_p(2\Delta t), \ldots, x_p(L_p\Delta t)]$, according to relation Eq. (3) of length $L_p \geq 50$ for the three

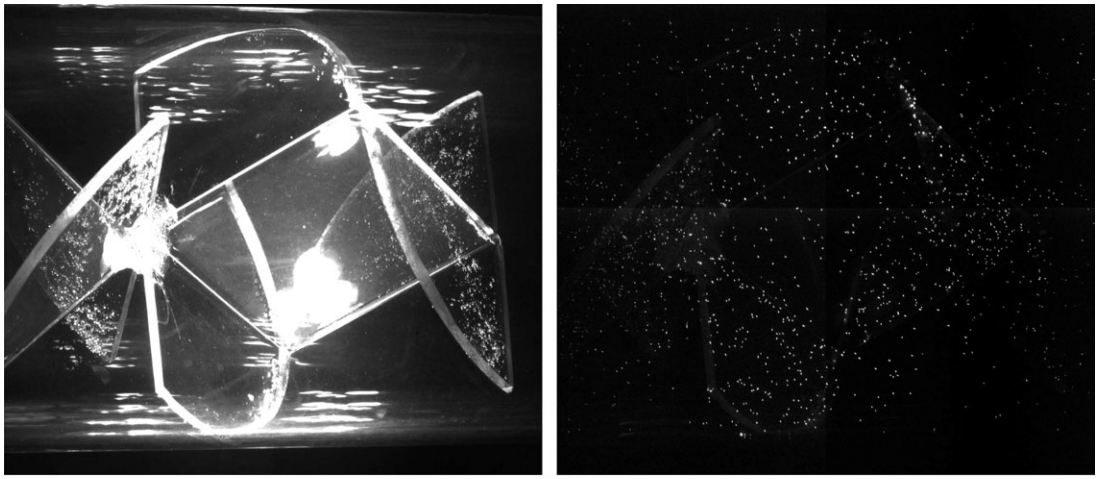

(a) (b)

Figure 7. Reduction of the optical distortion by reflections using optical filters: (a) original (unfiltered) image; (b) filtered image revealing fluorescent particles.

measurement regions combined.* (Tracks of length $L_p < 50$ have been discarded.) The distribution of track lengths L_p is shown in Figure 8a in terms of number of tracks N_p of a given length L_p and closely follows the correlation $N_p = cL_p^a$, with $c = 3.0892 \cdot 10^8$ and $a = -2.6587$ (solid line). This signifies an exponential decay in track lengths ($dN_p/dL_p = aN_p/L_p < 0$) and amounts to a mean track length of $\overline{L}_p = 120$ time levels. Note that the sudden increase in number of tracks for the highest length range is due to particles stuck on the tube wall and internal elements. These particles are easy to track yet their "trajectories," albeit physically correct, are irrelevant for the flow analysis. Hence, they are excluded from the correlation. This reveals that trajectories typically span time intervals considerably shorter than the duration of the measurement yet nonetheless cover a few hundred frames. For a typical displacement of 300 μm between consecutive frames, this leads to track lengths in the order of the characteristic length scale of the flow domain. This demonstrates that, though consistent tracking and matching of individual particles throughout the full sequence of frames proves difficult, the 3-DPTV algorithm performs well by enabling reliable measurement of substantial portions of the 3-D streamline pattern. This is discussed in more detail below.

Performance of the 3-DPTV algorithm depends, besides on time, also on space in that the majority of isolated trajectories is located in front of the internal elements (i.e., directly visible by the cameras through the tube wall). This is demonstrated in Figures 8b,c, showing the trajectories on the front and rear sides of the element, respectively. The cause for this must not be sought in refraction by the flat portions of the internal elements; this has been ruled out in section *Refraction at the Tube Wall and Internal Elements* as significant error source. However, not included in that analysis are the sharp edges at which constituent segments of an internal element join. These edges in fact constitute optical discontinuities that are basically impenetrable to light and, in consequence, appear as black stripes crisscrossing the images in various directions. Particles cannot be reliably tracked across such stripes, which, given they appear at different orientations in different camera views, severely restricts the unobstructed fields of view in the rear-side area of the flow domain. Hence, the substantially less and shorter trajectories in this subregion compared to the front-side area of the element.

*In this representation, $t = 0$ and $t = L_p\Delta t$ coincide with the time levels at which a certain particle p is first and last matched, respectively. This may differ from the sampling time levels $t_i = i\Delta t$.

Measurement of 3-D Flow Field and 3-D Streamline Pattern

Inlet velocity field

The performance and potential of the current 3-DPTV method for 3-D flow measurements in inline mixers is investigated by way of a comparative analysis between experimental results and numerical predictions. This analysis embarks on determination of the velocity distribution at the inlet $z = 0$ of the flow domain (Figure 1) so as to prescribe physically accurate boundary conditions for the numerical simulations (sections *Representative Case Study and Numerical Methods and Laboratory set-up*). The 3-D velocity at the inlet is evaluated from 3-D flow measurements in the inlet region. Its analysis reveals an axial velocity component u_z that clearly dominates over the transverse components $u_{x,y}$ and is axisymmetric [i.e., $u_z = u_z(r)$]. Figure 9a gives the axial component u_z as a function of the radius $r = \sqrt{x^2 + y^2}$ of 2-D positions (x,y) of data points in the 3-DPTV data set (crosses) in the inlet $z = 0$. The flattening of the profile in the center signifies a flow in its developing stage toward a fully developed Poiseuille profile.[47] These properties are consistent with a developing velocity field in an open tube (the inlet sits within the development length $L_e \approx 1.6\ m$ of a Poiseuille profile for a Newtonian fluid; section *Laboratory set-up*) and, thus, constitute first evidence of reliable measurements.

The measured axial profile admits straightforward approximation by the functional relation $u_z = U(q+2)(1 - |r/R|^q)/q$, with $q = (n + 1)/n$ and n a shape parameter. Least-squares fitting gives $n = 0.32$ and yields the solid curve in Figure 9a; the departure $\Delta u_z = u_{z,a} - u_{z,e}$ between analytical ($u_{z,a}$) and experimental ($u_{z,e}$) profiles is shown in Figure 9b (mean $\mu_{\Delta u} = 0.28$ mm/s and standard deviation $\sigma_{\Delta u} = 0.40$ mm/s) and stays within the $2\sigma_{\Delta u}$-limit indicated by the error bars in Figure 9a. It must be noted that an alternative representation based on standard polynomial fitting may slightly diminish

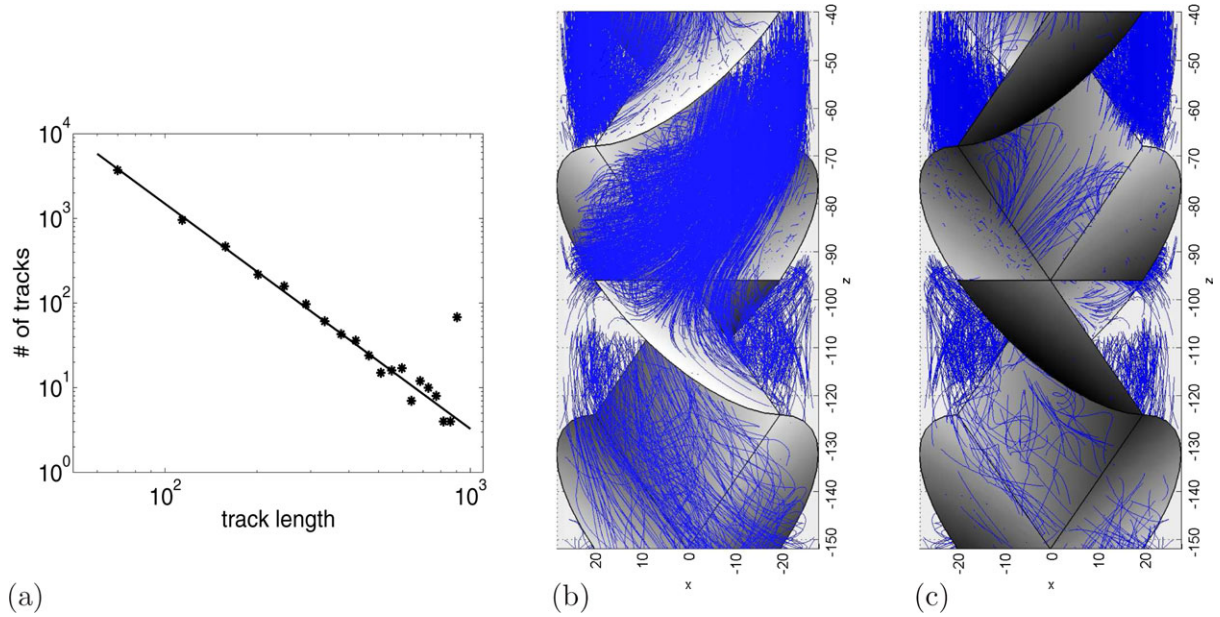

Figure 8. Performance of the 3-DPTV measurement and tracking procedure: (a) length distribution in the data set of about 6000 tracks; (b) tracks in the front-side area of the internal elements; and (c) tracks in the rear-side area of the internal elements.

[Color figure can be viewed in the online version, which is available at wileyonlinelibrary.com.]

the mean departure $\mu_{\Delta u}$ yet, in contrast with the above (strictly monotonic) functional form, suffers from oscillations in the profile that become more profound with increasing polynomial degree. Hence, the present study, notwithstanding the small deviation around $r \approx 15$ mm, adopts this functional form for the numerical model.

Internal 3-D velocity field

The 3-D experimental velocity field in the entire mixer is assembled from data sets obtained separately for the inlet, mixing, and outlet regions (section *General Tracking Performance*). Figure 10 shows the measured field (left column) in comparison with numerical predictions (right column) from downstream (top) and upstream (bottom) perspectives. The displayed 3-DPTV data correspond to about 4500 actual measurement positions distributed evenly throughout the flow domain and belong to a denser set of nearly 18,000 velocity vectors determined from the tracking results; the FLUENT data set corresponds to nodal values and is of comparable size. The velocity fields exhibit a good qualitative agreement; essential flow features as transition from the uniform inlet flow into a 3-D flow at the upstream element, the internal 3-D flow around the elements, and the swirl flow exiting the downstream element are recovered well by the 3-DPTV measurements.

Quantitative comparison between experimental and simulated velocity fields is carried out for the three measurement regions in two ways: (1) directly in the 3-DPTV data points; and (2) in representative cross-sections. To this end, data have been interpolated onto evaluation points by way of built-in MATLAB interpolation schemes. Figure 11 gives the experimental velocity field u_e (blue) and corresponding numerical prediction u_n (red) at the 3-DPTV measurement positions of Figure 10 in said flow regions in perspective (top) and projected (center) views. This reveals that, save occasional mismatches, experimental and numerical vector

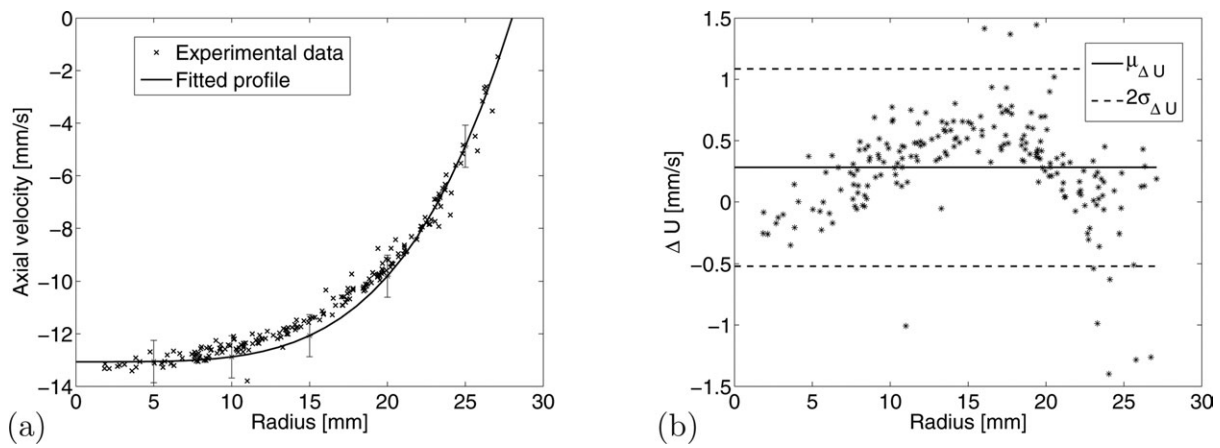

Figure 9. Developing inlet velocity profile ($z = 0$): (a) measured profile and its approximation by the functional relation $u_z = U(q + 2)(1 - |r/R|^q)/q$ ($q = (n + 1)/n$ and $n = 0.32$); (b) approximation error.

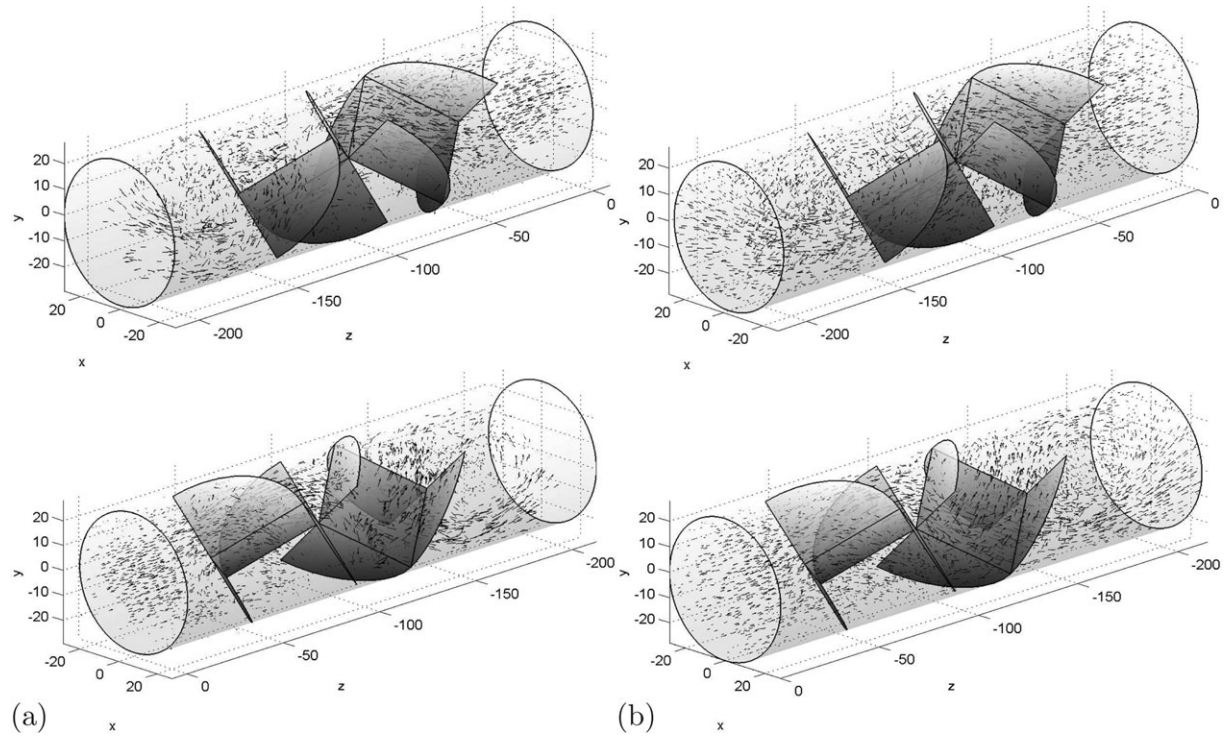

Figure 10. Measured vs. simulated 3-D velocity field: (a) 3-DPTV measurement positions; (b) nodal vectors by FLUENT.

fields are also on this detailed level in close correspondence. The deviation is quantified via $\epsilon_u \equiv |u_n - u_e|/|u_{e,max}|$ and represented per histogram in Figure 11 (bottom) for each flow region. (Note that the histograms are evaluated with the aforementioned denser 3-DPTV data set of about 18,000 positions.) The associated statistics read $\mu = 3/6/17\%$ (mean), $m = 2/4/13\%$ (median), and $\sigma = 6/9/14\%$ (standard deviation) for the inlet/mixing/outlet regions, signifying an overall good performance, in particular in the light of the challenges posed by the mixer geometry to the measurement method (section *Experimental Methods*). Strong outliers correspond primarily with spurious vectors due to particle mismatches by the ETH algorithm.

The relative deterioration in performance in mixing and outlet regions can in part be attributed to the more complex flow and geometry—and associated optical disturbances by the mixing elements—compared to the inlet region. However, a major cause for the deviations must be sought in two departures of the numerical model from the experimental configuration: the internal geometry and the outflow condition. (Recall that inflow conditions are closely matched.) The simulations use internal mixing elements consisting of infinitely thin plates with perfect shapes that seamlessly connect with the tube wall. The elements in the laboratory setup, on the other hand, are of finite thickness (3% of tube diameter), exhibit various imperfections (minute gaps with tube wall allowing weak "leakage" of fluid, rounded corners at joints of element segments) and are fixated via a downstream rod (diameter 1 mm) that spans the entire outlet region. The simulations impose a pressure outlet 60 mm downstream of the trailing element; the outlet section in the experimental apparatus covers about 800 mm and includes the flow-rate valve at 500 mm after the mixer exit. (The outflow section in the numerical model is restricted for computational efficiency.) These differences are consistent with the gradual increase in deviation ε_u in downstream direction. Further minor error sources are positioning uncertainties of calibration grid and mixing elements.

Cross-sectional velocity profiles have been determined in the inlet region at $z = 30$ mm (10 mm before upstream element), in the mixing region at $z = 68$ mm (midplane of upstream element), and in the outlet region at $z = 172$ mm (20 mm after downstream element). Figure 12 gives the cross-sectional profile near the inlet for the three velocity components obtained from experimental data (top) and via numerical simulations (bottom). This exposes an overall close quantitative agreement between measurements and predictions. The axial velocity u_z is strongly axisymmetric and close to that found before (Figure 9). The slight noncircularity of the contours signifies a breakdown of axisymmetry due to the onset of 3-D flow induced by the upstream element. Note that this subtle feature is present in the experimental field as well. The transition to 3-D flow manifests itself in weak transverse circulations that give rise to the asymmetries in the transverse components $u_{x,y}$ clearly visible in shown profiles. The comparably poor definition of the transverse components $u_{x,y}$ must be attributed to their small magnitude relative to the axial flow: $u_{x,y}/u_z \sim \mathcal{O}(10\%)$. This renders the former more susceptible to noise.

The cross-sectional profile in the midplane of the upstream element is shown in Figure 13. This reveals two large-scale transverse circulation zones separated by the mixing element, roughly coinciding with the downward-sloping bar in Figure 13c, and two localized recirculation zones, demarcated by the small patches of approximately uniform color. These features, including the two peaks in the vertical component u_y (dark regions in the red area in Figure 13b), are well resolved by the experimental field. This again demonstrates the good agreement between 3-DPTV results and numerical simulations that, despite the more complex flow, in fact exceeds that of the above inlet region due to a relatively

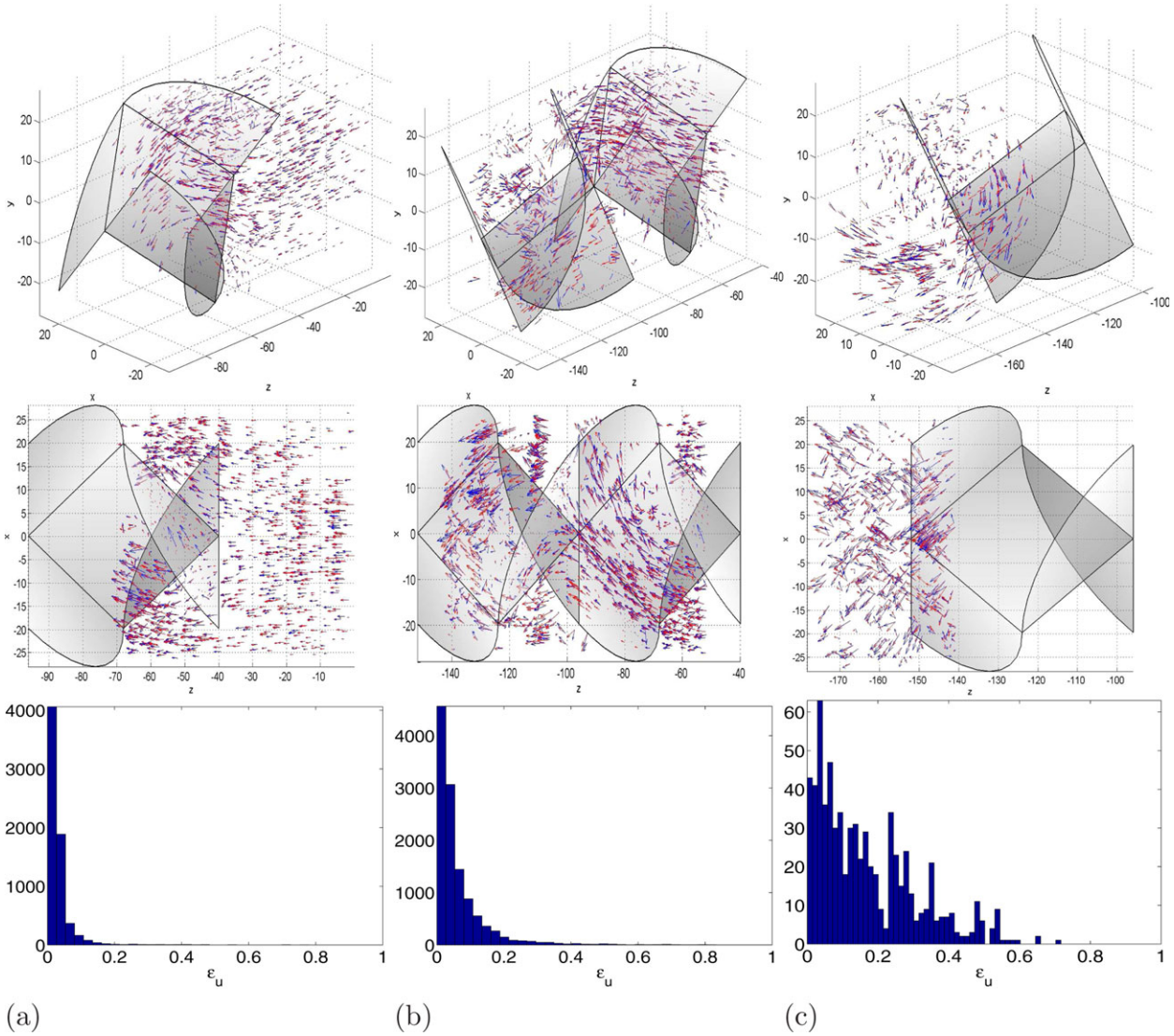

Figure 11. Measured (blue) vs. simulated (red) 3-D velocity field in each of the measurement regions: (a) inlet region; (b) mixing region; and (c) outlet region.

The histograms give the distribution of the deviation ϵ_u between experimental and numerical fields in each region. [Color figure can be viewed in the online version, which is available at wileyonlinelibrary.com.]

dense data set in this area. Its inhomogeneous distribution is considered the primary cause for the somewhat poorer resolution of $u_{x,y}$ in the region to the left of the mixing element. Note that, compared to the inlet cross-section (Figure 12), the definition of flow features is of equal quality for all velocity components.

Figure 14 gives the velocity components in the outlet region. The transverse components $u_{x,y}$ are of the same magnitude as the axial flow u_z, which, consistent with Figures 10 and 11c, signifies a strong exit swirl. However, the nonzero areas of the vertical component u_y being substantially more localized than those of the horizontal component u_x implies that the swirl flow is still developing. This phenomenon is picked up well by the experiments. Moreover, smaller-scale features are still reasonably resolved yet overall agreement between measured and simulated field (of in particular the axial component) is less compared to inlet and mixing regions due the differences between numerical model and experimental setup outlined before.

Internal 3-D streamline pattern

The 3-D streamline pattern within the mixer can, in contrast with the velocity field, be obtained only region-wise for the inlet, mixing, and outlet regions (section *General Tracking Performance*). Moreover, mixing flows exhibit (locally) chaotic advection, that is, the repeated stretching and folding of material regions, implying that individual streamlines are extremely sensitive to initial conditions in the sense that minute deviations in initial tracer positions may lead to dramatic differences in streamlines.[39,48] This property renders a comparison between experiments and simulations on the basis of individual streamlines impractical and, in fact, of limited use. However, continuity organizes streamlines into larger-scale coherent structures that, in contrast with their individual constituent streamlines, are structurally stable and robustly detectable. Such coherent structures impose geometrical constraints on the fluid motion and are key to the transport (and mixing) properties of a flow.[4,34,39] Coherent structures of particular

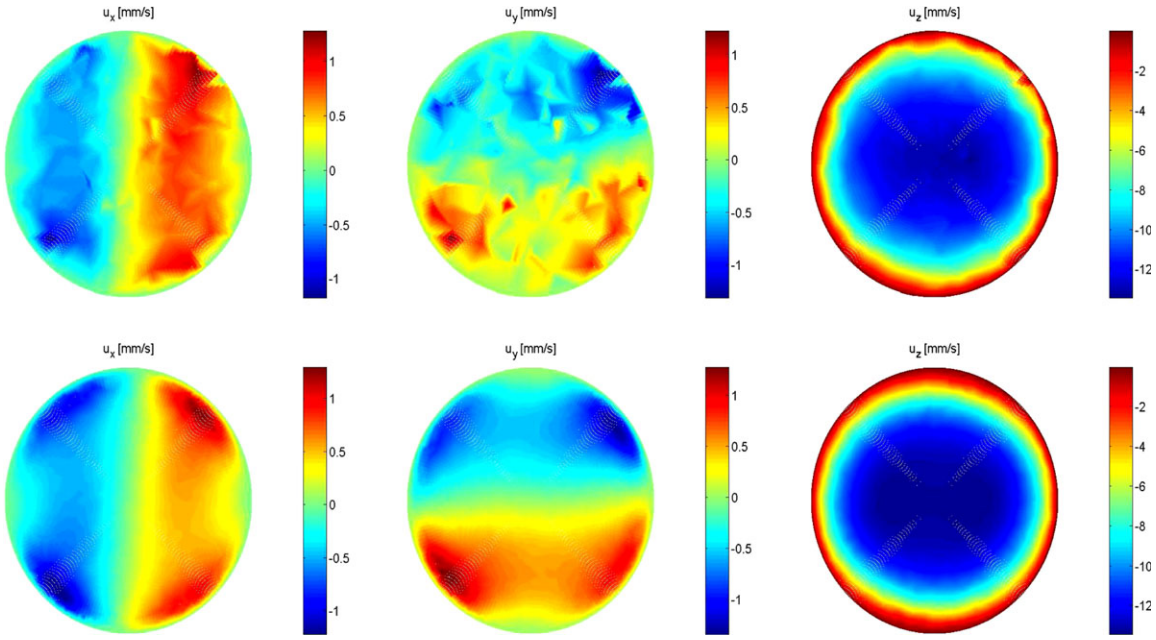

Figure 12. Cross-sectional velocity in the inlet region at $z = 30$ mm (viewing xy-plane in $+z$ direction) according to 3-DPTV measurements (top) and numerical simulations (bottom).

[Color figure can be viewed in the online version, which is available at wileyonlinelibrary.com.]

relevance to inline mixers include families of concentric stream tubes and chaotic regions. The former restrict fluid to confined areas within the cross-section and, thus, constitute transport barriers and, in consequence, poor-mixing zones; the latter accomplish rapid lateral spreading of material in the throughflow and, thus, promote efficient mixing.[4,21,39] Hence, 3-D experimental transport studies should concentrate on the formation of coherent structures and geometric composition of 3-D streamline patterns instead of on individual streamlines.[†] This approach provides the more complete—and, given the robustness of coherent structures to, for example, measurement inaccuracies, more reliable—picture on mixing and transport properties. The present study takes a first step in that direction by a comparative analysis of some larger-scale flow features.

Figure 15 gives the experimental streamlines of all regions combined (blue) in comparison to their simulated counterparts (red) from various perspectives. This exposes a larger-scale coherence in the streamline pattern that comprises flow features as the deflection of the throughflow by the upstream element, the internal mixing pattern, and the exit swirl. The global geometric compositions according to measurements and predictions, despite significant divergence between some individual streamlines on account of the aforementioned sensitivity to initial positions, exhibit a good qualitative agreement. Clusters of experimental streamlines effectively "shadow" their simulated counterparts. Two important flow features, namely the internal mixing pattern and the exit swirl, are investigated in more detail below.

The basic mixing principle of the current configuration is the systematic transverse reorientation of the axial throughflow by an element-wise division into two adjacent streams with alternating rotations in the cross-section. Principal objective is the accomplishment of chaotic fluid motion for the purpose of rapid lateral distribution of material. This process is visualized in Figure 16 by the fluid stream passing one side of the upstream element, where blue and red again represent experimental and numerical streamlines, respectively. Note that experimental streamlines are truncated near the leading edge of the downstream element due to the partitioning of the flow domain into three measurement regions (section *General Tracking Performance*). The streamlines undergo a strong lateral dispersion due to vortical motion triggered by the leading elliptical segment of the upstream element and bifurcation of the remaining fluid stream by its impingement on the leading elliptical segment of the downstream element. The separation of the incoming fluid stream into vortical structures and a bifurcating "jet" is particularly apparent in the bottom panels of Figure 16. These coherent structures are present in both the experimental and numerical streamline patterns and exhibit a strong correlation to a great level of detail. This validates the current analysis both ways by implying an accurate resolution of the 3-D flow structure by both the 3-DPTV experiments and the numerical model. The 3-DPTV streamlines, thus, yield a first experimental characterization of the 3-D internal mixing pattern of an industrial static mixer. The observed lateral dispersion is indicative of chaotic advection—and efficient mixing—yet existence of (localized) stream tubes cannot be conclusively ruled out at this stage.

The flow enters an open tube after exiting the mixing region, initiating its development into a Poiseuille flow. This gives rise to the exit swirl found before (section *Internal 3-D velocity field*) and manifests itself in the formation of a vortical structure emerging from the downstream element that span the entire cross-section. Figure 17 demonstrates this for the fluid stream passing one side of the downstream mixing element. The streamlines, on emanating from the

[†]Exactly determining which physical streamline emanates from a certain initial position is in a chaotic system basically impossible due to a, in practice, only finite precision. However, the shadowing lemma from dynamical-systems theory states that simulated or measured trajectories always closely follow some physical trajectory.[49] Hence, a sufficiently dense set of initial conditions, irrespective of their exact locations, yields a web of streamlines that demarcates any coherent structures and, thus, invariably exposes the geometric organization of the streamline pattern.

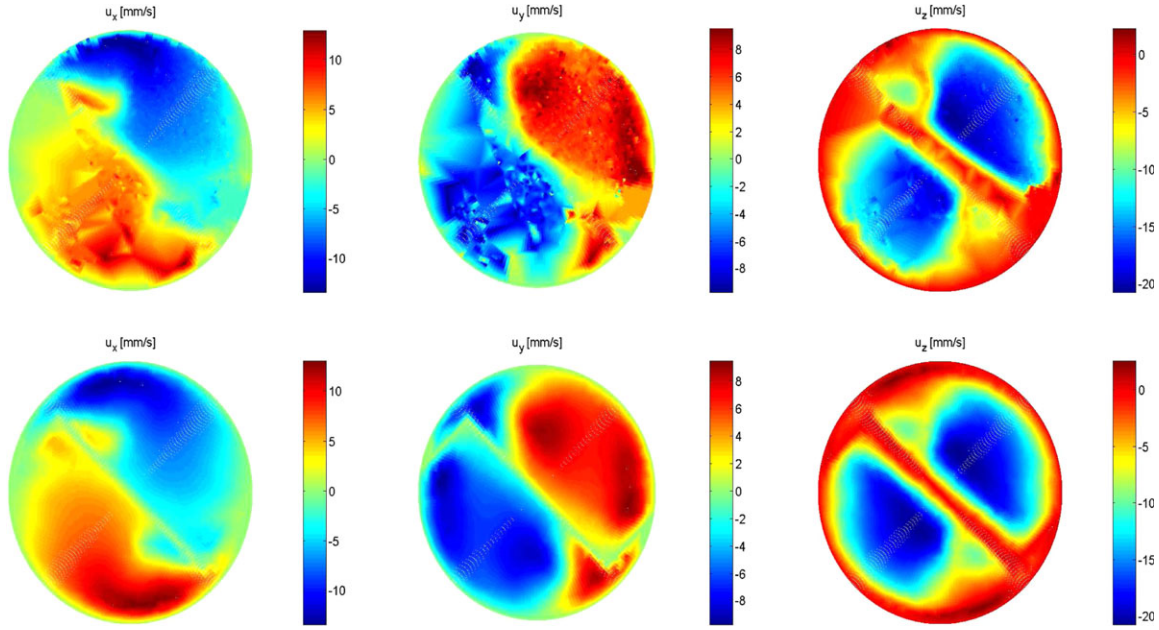

Figure 13. Cross-sectional velocity in the mixing region at z = 68 mm (viewing xy-plane in $+z$ direction) according to 3-DPTV measurements (top) and numerical simulations (bottom).

[Color figures can be viewed in the online version, which is available at wileyonlinelibrary.com.]

latter, develop into an outwardly spiralling vortical structure that gradually transits into the characteristic helical streamlines of exit swirls. Note that this spiralling becomes more profound the closer the streamlines are to the mixing element. The correlation between the coherent structures in the experimental (blue) and numerical (red) streamlines, similar to the mixing pattern, is again strong, offering further evidence of the accuracy, and reliability of the 3-DPTV measurements.

Conclusions

The present study describes the experimental characterization of the 3-D laminar flow and corresponding 3-D streamline pattern in a representative industrial static mixer by way of 3-D 3-DPTV. Laminar flow and the staticmixing principle are two key elements in a wide range of industrial mixing and heat-transfer systems, encompassing (thermal) processing of viscous fluids, compact equipment for process intensification, as well as many emerging microfluidic applications.

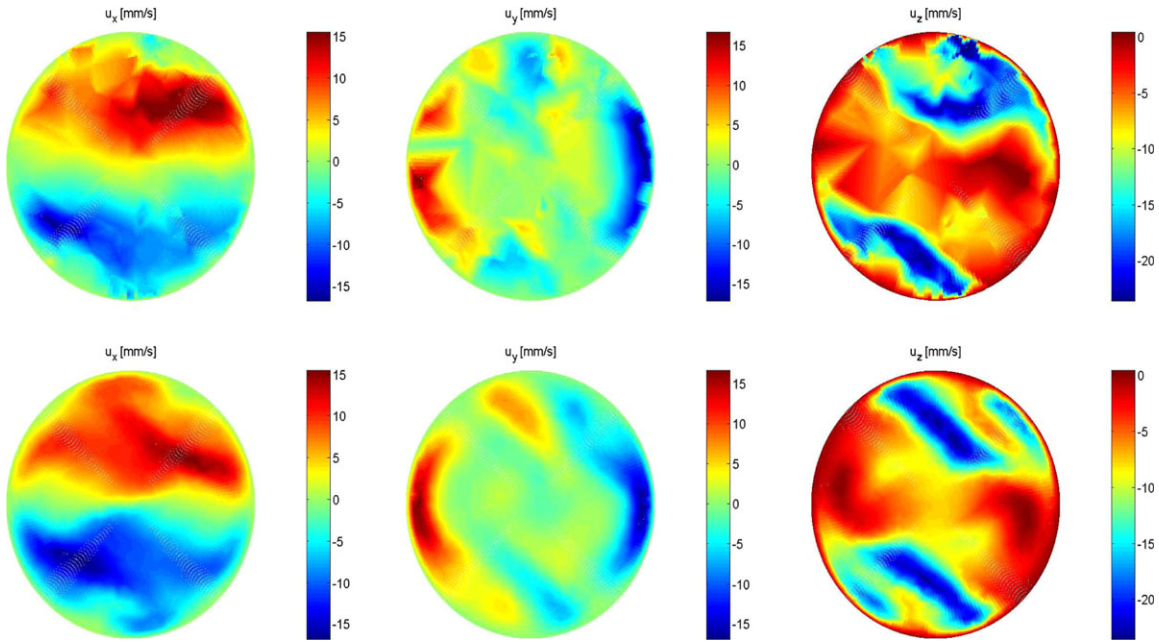

Figure 14. Cross-sectional velocity in the outlet region at z = 172 mm (viewing xy-plane in $+z$ direction) according to 3-DPTV measurements (top) and numerical simulations (bottom).

[Color figures can be viewed in the online version, which is available at wileyonlinelibrary.com.]

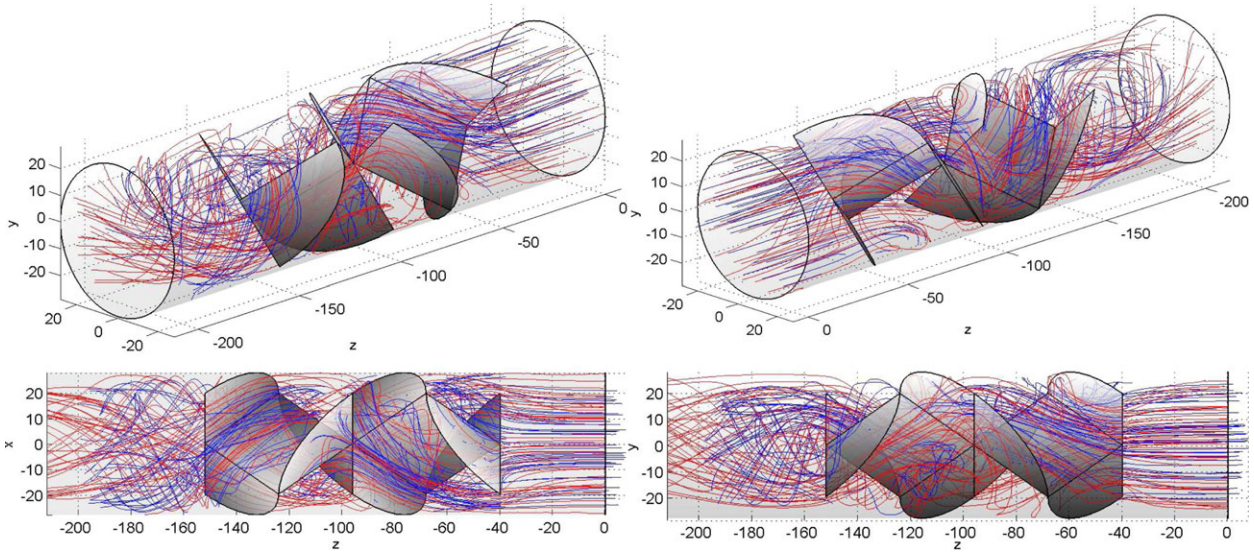

Figure 15. Measured (blue) vs. simulated (red) 3-D streamlines in the entire flow domain.

[Color figures can be viewed in the online version, which is available at wileyonlinelibrary.com.]

Key challenge for performance of 3-DPTV measurements in static mixers is the geometrical complexity of the flow domain due to the cylindrical outer wall and internal mixing elements. This introduces two optical distortions: refraction and reflections at curved and internal walls. Tackling of these issues is essential for reliable determination of the 3-D flow field and fluid trajectories. Refraction is dealt with by placement of the domain of interest in a cubical viewing box. This reduces the optical deformation by the mixer geometry from nearly 25% to about 1%, which is considered acceptable. Refraction by the bounding walls of the viewing box is accounted for by the 3-DPTV image-processing algorithm. Reflections are eliminated by employment of fluorescent tracer particles and their illumination by a dedicated light source (LEDs), which enables separation of former and latter through optical filtering. Key to the measurement strategy proposed in this study is the particular combination of these optical techniques with the 3-DPTV data-processing algorithm introduced before.

The proposed measurement strategy exhibits a good general tracking performance. Typical measurements involve 900–1000 frames with nearly 200 tracer particles each. An average matching yield of ~76% is attained and results in a combined set of 6000 tracks with a length of 50 frames or more at an average of 120 frames. This enables adequate experimental characterization of the 3-D flow field and the

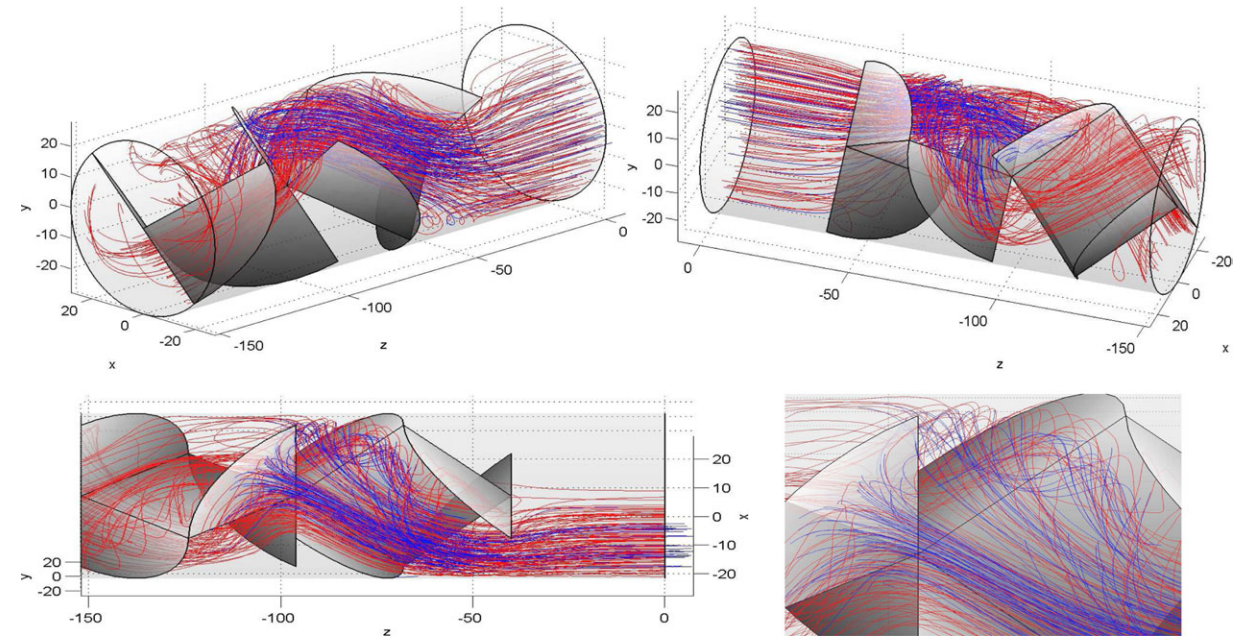

Figure 16. Visualization of the internal mixing pattern by trajectories passing one side of the upstream element: 3-DPTV measurements (blue) vs. numerical simulations (red).

[Color figure can be viewed in the online version, which is available at wileyonlinelibrary.com.]

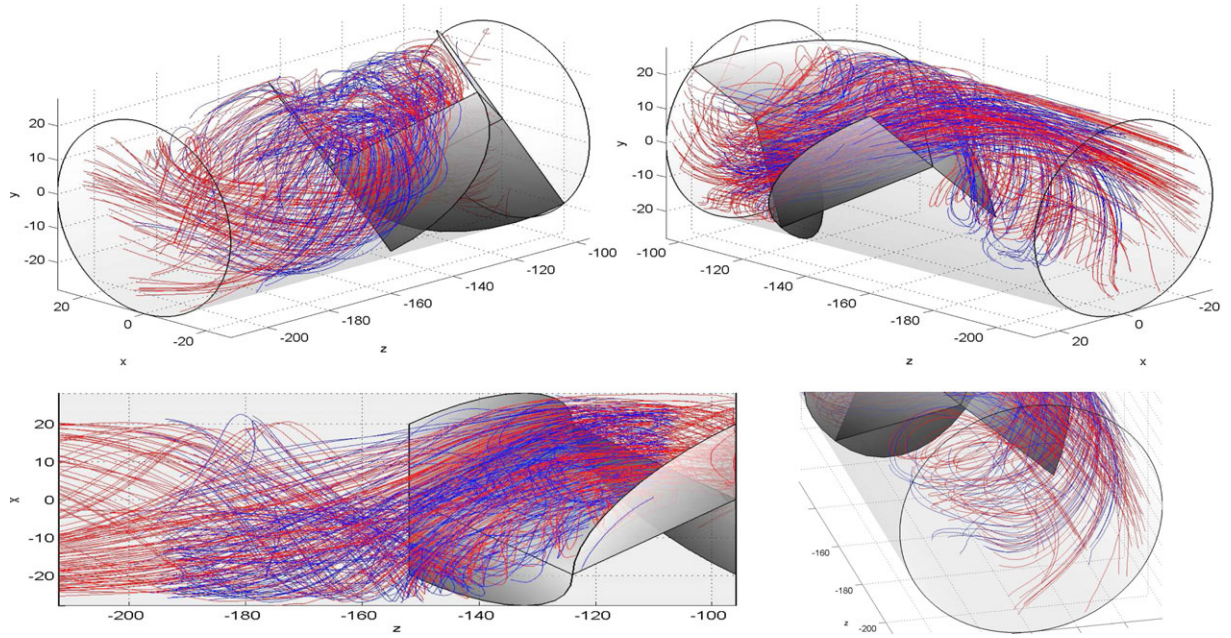

Figure 17. Visualization of the exit swirl by trajectories passing one side of the downstream element: 3-DPTV measurements (blue) vs. numerical simulations (red).

[Color figure can be viewed in the online version, which is available at wileyonlinelibrary.com.]

3-D streamline pattern. The analysis exposes a remaining optical issue: localized refraction at the sharp edges of the internal elements. These edges appear as dark ''stripes'' in the imagery that severely restrict the field of view in the rear-side area of the internal elements. This adversely affects the tracking performance and results in substantially less and shorter tracks in this flow region compared to the front-side area of the elements.

Comparative analysis of experimental results with numerical simulations reveals an overall good agreement. 3-D velocity vectors on average coincide within 10–15% and a major cause for deviations must be sought in two departures of the numerical model from the experimental configuration: (1) the internal geometry and (2) the outflow condition. Simulations use infinitely thin mixing elements of perfect shape and impose isobaric conditions at the outlet of the test section; the experimental setup, on the other hand, has elements of finite thickness and imperfect shape, a downstream fixation rod, and a valve near the outflow region. 3-D streamlines are compared on the basis of larger-scale coherent structures that form due to continuity. Such coherent structures impose geometrical constraints on the fluid motion and are key to the transport (and mixing) properties of a flow. Essential and complex 3-D structures as the internal mixing pattern induced by the mixing elements and the exit swirl are well recovered by the experimental study and in close agreement with numerical predictions.

The above findings imply that the 3-DPTV measurements accurately capture the 3-D flow field and streamline patterns throughout the entire mixer. The present study to the best of our knowledge is the first experimental characterization of truly 3-D flow and (basic) mixing phenomena within industrial static mixers. Thus, the adopted measurement strategy lays the groundwork for experimental flow studies in other industrial devices with complex geometry. Follow-up investigations are in progress and concern in-depth 3-D experimental mixing analyses by sophisticated data processing using Lagrangian concepts from laminar-mixing studies.[4,34,39] This expands on this study by further isolation and demarcation of coherent structures in the 3-D streamline patterns. Moreover, efforts for flow measurements under nonisothermal conditions are underway. This introduces a formidable optical issue: thermally induced refraction due to dependence of the local refractive index on the fluid density and, in turn, on the temperature field.

Acknowledgments

The authors greatly appreciate the technical support by Primix BV, Mijdrecht, The Netherlands, Henri Vliegen and Geert-Jan van Hoek of the Energy Technology Laboratory, Department of Mechanical Engineering (TU/e), and Ad Holten of the Fluid Dynamics Laboratory, Department of Applied Physics (TU/e).

Literature Cited

1. Metcalfe G, Lester D. Mixing and heat transfer of highly viscous food products with a continuous chaotic duct flow. *J Food Eng*. 2009;95:21–29.
2. Harnby N, Edwards M, Nienow A. *Mixing in the Process Industries*. Oxford: Butterworth-Heinemann, 1997.
3. Singh MK, Anderson PD, Speetjens MFM, Meijer H. Optimizing the rotated arc mixer. *AIChE J*. 2008;54:2809–2822.
4. Speetjens M, Metcalfe G, Rudman M. Topological mixing study of non-Newtonian duct flows. *Phys Fluids*. 2006;18:103103/1–11.
5. Kumar V, Shirke V, Nigam K. Performance of Kenics static mixer over a wide range of Reynolds numbers. *Chem Eng J*. 2008;139: 284–295.
6. Pustelnik P. Investigation of residence time distribution in Kenics static mixers. *Chem Eng Process*. 1986;20:147–154.
7. Yang HC. Mixing characteristics of motionless mixers. *J Vis*. 2007; 10:83–89.
8. Sundén B, Shah R. *Advances in Compact Heat Exchangers*. Philadelphia: Edwards, 2007.
9. Weinekötter R. Compact and efficient continuous mixing processes for production of food and pharmaceutical powders. *Trends Food Sci Technol*. 2009;20:S48–S50.
10. Beebe D, Mensing G, Walker G. Physics and applications of microfluidics in biology. *Annu Rev Biomed Eng*. 2002;4:261–286.
11. Hansen C, Quake S. Microfluidics in structural biology: smaller, faster … better. *Curr Opin Struct Biol*. 2003;13:538–544.

12. Stone HA, Stroock AD, Ajdari A. Engineering flows in small devices: microfluidics toward a lab-on-a-chip. *Annu Rev Fluid Mech*. 2004;36:381–411.
13. Thakur R, Vial C, Nigam K, Nauman E, Djelveh G. Static mixers in the process industries—a review. *Trans IChemE*. 2003;81: 787–826.
14. Laporte T, Wang C. Continuous processes for the production of pharmaceutical intermediates and active pharmaceutical ingredients. *Curr Opin Drug Discov Devel*. 2007;10:738–745.
15. Becht S, Franke R, Geisselmann A, Hahn H. Micro process technology as a means of process intensification. *Chem Eng Technol*. 2007; 30:295–299.
16. Anxionnaza Z, Cabassuda M, Gourdona C, Tochon P. Heat exchanger/reactors (HEX reactors): concepts, technologies: state-of-the-art. *Chem Eng Process*. 2008;47:2029–2050.
17. van Wageningen W, Kandhai D, Mudde R, van den Akker HEA. Dynamic flow in a Kenics static mixer. *AIChE J*. 2004;50:1684–1696.
18. Hobbs DM, Swanson PD, Muzzio FJ. Numerical characterization of low Reynolds number flow in the Kenics static mixer. *Chem Eng Sci*. 1998;53:1565–1584.
19. Galaktionov O, Anderson P, Peters G, Meijer H. Analysis and optimization of Kenics mixers. *Int Polymer Process*. 2003;18:138–150.
20. Byrde O, Sawley M. Optimization of a Kenics static mixer for non-creeping flow conditions. *Chem Eng J*. 1999;72:163–169.
21. Metcalfe G, Rudman M, Brydon A, Graham L, Hamilton R. Composing chaos: an experimental and computational study of an open duct mixing flow. *AIChE J*. 2006;52:9–28.
22. Hirech K, Arhaliass A, Legrand J. Experimental investigation of flow regimes in an SMX Sulzer static mixer. *Ind Eng Chem Res*. 2003;42:1478–1484.
23. Li H, Fasol C. Pressure drop of Newtonian and non-Newtonian fluids across a Sulzer SMX static mixer. *Trans IChemE*. 1997;75: 792–796.
24. Jaffer S, Wood P. Quantification of laminar mixing in the Kenics static mixer: an experimental study. *Can J Chem Eng*. 1998;76: 516–521.
25. Avalosse T, Crochet M. Finite-element three-dimensional simulation of mixing: 2. flow through a Kenics mixer. *AIChE J*. 1997; 43:588–597.
26. Wilneff J. A Spatio-Temporal Matching Algorithm for 3D Particle Tracking Velocimetry. ETH PhD Thesis, 15276, Institute of Environmental Engineering, Eidgenoessische Technische Hochschule (ETH) Zuerich, Switzerland, 2003.
27. Luethi B, Tsinober A, Kinzelbach W. Lagrangian measurement of vorticity dynamics in turbulent flow. *J Fluid Mech*. 2005; 528:87–118.
28. Holzner M, Liberzon A, Nikitin N, Lüthi B, Kinzelbach W, Tsinober A. A Lagrangian investigation of the small-scale features of turbulent entrainment through particle tracking and direct numerical simulation. *J Fluid Mech*. 2008;598:465–475.
29. Cheng Y, Diez FJ. A 4D Imaging tool for lagrangian particle tracking in stirred tanks. *AIChE J*. 2011;57:1983–1996.
30. Malik N, Dracos T, Papantoniou D. Particle tracking velocimetry in three-dimensional flows−Part II: particle tracking. *Exp Fluids*. 1993; 15:279–294.
31. Kreizer M, Ratner D, Liberzon A. Real-time image processing for particle tracking velocimetry. *Exp Fluids*. 2010;48:105–110.
32. Dore V, Moroni M, Menach ML, Cenedese A. Investigation of penetrative convection in stratified fluids through 3D-PTV. *Exp Fluids*. 2009;47:811–825.
33. Otto F, Riegler E, Voth G. Measurements of the steady streaming flow around oscillating spheres using three dimensional particle tracking velocimetry. *Phys Fluids*. 2008;20:093304.
34. Speetjens MFM, Clercx HJH, van Heijst GJF. A numerical and experimental study on advection in three-dimensional Stokes flows. *J Fluid Mech*. 2004;514:77–105.
35. Nishimura M, Ueno I, Nishino K, Kawamura H. 3D PTV measurement of oscillatory thermocapillary convection in half-zone liquid bridge. *Exp Fluids*. 2005;38:285–290.
36. Walpot R, Rosielle P, van der Geld C. Design of a set-up for high-accuracy 3D PTV measurements in turbulent pipe flow. *Meas Sci-Technol*. 2006;17:3015–3026.
37. Pedocchi F, Martin J, Garcy M. Inexpensive fluorescent particles for large-scale experiments using particle image velocimetry. *Exp Fluids*. 2008;45:183–186.
38. Blaj O, Merzeau P, Snabre P, Pouligny B. An automated single-particle tracker: application to characterization of non-azimuthal motion in Couette flows at low Reynolds number. *Exp Fluids*. 2011;50:1559–1570.
39. Ottino JM. *The Kinematics of Mixing: Stretching, Chaos, and Transport*. Cambridge: Cambridge University Press, 1989.
40. Raffel M, Wereley CWS, Kompenhans J. *Particle Image Velocimetry—A Practical Guide*. Berlin: Springer, 2007.
41. Shah R, London A. *Laminar Flow Forced Convection in Ducts*. New York: Academic Press, 1978.
42. Ouellette N, Xu H, Bodenschatz E. A quantitative study of three-dimensional Lagrangian particle tracking algorithms. *Exp Fluids*. 2006;40:301–313.
43. Chang T, Taterson G. Application of image processing to the analysis of three-dimensional flow fields. *Opt Eng*. 1983;32:283–287.
44. Hecht E. *Optics*. San Francisco: Addison Wesley, 2002.
45. Coppeta J, Rogers C. Dual emission laser induced fluorescence for direct planar scalar behavior measurements. *Exp Fluids*. 1998;25: 115.
46. Sidney RF. *Applied Photographic Optics*. Oxford: Focal Press, 2002.
47. Kundu P. *Fluid Mechanics*. San Diego: Academic Press, 1990.
48. Ott E. *Chaos in Dynamical Systems*. Cambridge: Cambridge University Press, 2002.
49. Grebogi C, Hammel S, Yorke J, Sauer T. Shadowing of physical trajectories in chaotic dynamics: containment and refinement. *Phys Rev Lett*. 1990;65:1527–1530.

Manuscript received Dec. 16, 2011, revision received Jun. 4, 2012, and final revision received Sept. 26, 2012.